Materials Horizons

ROYAL SOCIETY OF CHEMISTRY

COMMUNICATION

View Article Online
View Journal | View Issue

Check for updates

Cite this: *Mater. Horiz.*, 2026, 13, 3451

Received 29th November 2025,
Accepted 20th January 2026

DOI: 10.1039/d5mh02273h

rsc.li/materials-horizons

Structurally tailored nanocomposite sorbent enabling high-energy-density thermochemical storage in e-thermal banks for electric vehicle applications

Waseem Aftab, * Muhammad Khurram, Qiqiu Huang, Dacheng Li, Muhammad Maqbool, Jiatong Jiang and Yongliang Li*

Electric vehicles (EVs) experience substantial reductions in driving range under extreme weather conditions—primarily due to the energy demands of cabin climate control (up to ~54%) and, to a lesser extent, battery inefficiencies (~20%). To address this issue, we propose an auxiliary energy source termed as an e-thermal bank, designed to support onboard heating, ventilation, and air conditioning (HVAC) and battery thermal management (BTM). The e-thermal bank is a high-energy-density, microwave-driven, fast-charging thermochemical storage (TCS) system that simultaneously manages cabin climate and battery temperature. To meet the stringent performance requirements of this innovative system, its key component—an advanced sorbent material—is developed through confinement of a TCS salt into a micro- and macro-structured porous matrix. The resulting optimized sorbent exhibits a high sorption capacity of 3.96 g g^{-1}, a rapid sorption rate, and a record-high material-level energy density of 10 426 kJ g^{-1} at 90% relative humidity (RH), all the while ensuring leak-proof operation. Thanks to its structural stability and scalability, this performance translates effectively into a prototype system achieving an ultra-high energy density of 2135 Wh kg^{-1} and power densities of 2.96 kW kg^{-1} for heating and 3.016 kW kg^{-1} for cooling. Theoretical evaluations based on real-world datasets indicate that incorporating the e-thermal bank could extend EV driving range by approximately 30% in winter and 20% in summer across most global regions.

New concepts

Electric vehicles (EVs) suffer severe efficiency losses in extreme climates because their battery packs must simultaneously power propulsion, cabin HVAC, and battery thermal management. We introduce a fundamentally new concept—an auxiliary microwave-driven thermochemical energy storage system (an "e-thermal bank")—that decouples thermal management from the traction battery. This concept represents the first integration of a fast-charging, high-energy-density thermochemical storage (TCS) technology designed specifically to support both heating and cooling demands in EVs. The breakthrough lies in the structural engineering of a nanocomposite sorbent, where TCS salts are confined within a micro- and macro-structured matrix to deliver unprecedented performance: a sorption capacity of 3.96 g g^{-1} and a record material-level energy density of 10.4 kJ g^{-1} at 90% RH, coupled with leak-proof and scalable operation. By translating this material innovation into a prototype system with ultra-high energy and power densities for both heating and cooling, our work provides new insight into thermochemical storage as a practical, high-power thermal battery for EV applications. System-level analyses further reveal its transformative potential—enabling 20–30% extension of EV driving range across diverse climatic regions. This concept reframes thermochemical storage as a core enabler of next-generation sustainable mobility.

Introduction

Electric vehicles (EVs) are crucial to achieving global net-zero emissions. According to the International Energy Agency's Global Electric Vehicle Outlook 2024, the EV market grew by over 25% in 2024, reaching more than 17 million EVs worldwide. This expansion is expected to continue in the coming decades. Currently, most EVs rely on a single primary energy source—the electric battery pack—which powers both the propulsion system and the heating, ventilation, and air conditioning (HVAC) system through resistive heating and vapor compression cooling. This dual demand leads to a significant reduction in driving range, with losses of up to 30% in summer and up to 54% in winter.[1–4] These reductions stem primarily from increased energy consumption and, to a lesser extent, battery inefficiencies.[3] To enhance energy efficiency, many modern EVs are now equipped with heat pump technology, particularly in moderately cold climates.[5,6] However, they still require electrical energy to operate, consuming onboard battery capacity and resulting in limited improvement in the cruising range. Range anxiety—the fear that an EV battery will deplete mid-trip without access to a charging

Birmingham Centre for Energy Storage (BCES) & School of Chemical Engineering, University of Birmingham, Birmingham B15 2TT, UK. E-mail: w.aftab@bham.ac.uk, y.li.1@bham.ac.uk

station—remains a major barrier to widespread EV adoption. Additionally, the battery pack accounts for 45–50% of an EV's total cost, making its use for HVAC both inefficient and economically impractical.[7] Addressing these challenges is essential to improving EV efficiency, reducing range anxiety, and accelerating global EV adoption. A promising strategy to mitigate the reduction in driving range under unfavourable weather conditions is integrating a secondary onboard energy source for HVAC, rather than relying solely on the electric battery-powered HVAC system.[8,9] In this context, we propose the e-thermal bank, an electricity-driven, sorption-based thermochemical storage (TCS) system designed for onboard EV HVAC applications. Unlike conventional TCS technologies, the e-thermal bank represents an electrified thermochemical storage platform tailored for mobile use, capable of meeting both heating and cooling demands while offering fast response, high energy density, and synergistic integration with the battery thermal management (BTM) system. The operational details of the e-thermal bank are described in Fig. S1.

More broadly, TCS represents a rapidly advancing class of thermal energy storage technologies, characterized by its exceptionally high energy density—exceeding 2–3 MJ kg^{-1}—which is several orders of magnitude greater than that of sensible and latent heat storage systems, and approximately 5–6 times higher than that of commercial lithium-ion batteries.[10,11] Beyond its storage density, TCS also offers the advantages of long-term energy retention with minimal thermal losses compared with other thermal storage technologies. The performance of a TCS system is governed by coupled (de)sorption reactions and heat/mass transfer, which directly impact critical metrics such as specific power, energy density, thermal efficiency, and stability. Achieving an efficient TCS system requires high-performance sorbent materials with exceptional sorbate uptake capacity, high enthalpy, efficient heat and mass transfer properties, moderate desorption temperatures, and scalable production.[12,13] Traditional physisorbents, such as silica gel and zeolites, are limited by their low sorbate uptake capacity,[14] while emerging metal–organic frameworks (MOFs) face challenges related to thermal and hydrolytic stability, as well as large-scale production constraints.[15,16] Chemisorptive salts, in contrast, offer superior sorption capacity, higher enthalpy, lower desorption temperatures, and cost-effectiveness.[17–19] Among various hygroscopic salts, calcium chloride ($CaCl_2$) stands out due to its low cost, high hygroscopicity, exceptionally high energy density, and dual functionality, making it suitable for both heating and evaporative cooling. Specifically, heat storage/release is governed by the reversible hydration/dehydration of $CaCl_2$, enabling thermal energy to be stored in the form of chemical potential. During charging (regeneration), $CaCl_2{\cdot}nH_2O$ undergoes dehydration to anhydrous $CaCl_2$ with release of water vapour. During discharging, the reverse hydration proceeds through a multi-step moisture uptake pathway, including initial solid–gas chemisorption, followed by deliquescence and subsequent liquid-phase absorption, as described by the following reactions.[20,21]

$$\text{Chemisorption}\quad CaCl_2(s) + 4H_2O(g) \rightleftharpoons CaCl_2{\cdot}4H_2O(s) + \text{Heat} \tag{1}$$

$$\text{Deliquescence}\quad CaCl_2{\cdot}4H_2O(s) + 2H_2O(g) \rightleftharpoons CaCl_2{\cdot}6H_2O(aq) + \text{Heat} \tag{2}$$

$$\text{Solution absorption}\quad CaCl_2{\cdot}6H_2O(aq) + xH_2O(g) \rightleftharpoons CaCl_2{\cdot}nH_2O(aq) + \text{Heat} \tag{3}$$

Similar to other thermochemical sorbents, $CaCl_2$ enables controllable thermal energy storage as long as it is isolated from humid conditions in the charged (anhydrous) state. During discharging, anhydrous $CaCl_2$ hydrates sequentially depending on vapour pressure (relative humidity, RH), accompanied by heat release. At high RH, deliquescence leads to concentrated $CaCl_2$ brine formation, and the RH-dependent equilibrium limit suggests a theoretical maximum uptake of $\sim$8.6 g g^{-1} at 90% RH. However, its susceptibility to leak and agglomerate during deliquescence reduces mass transfer efficiency over multiple cycles.[22,23] Recent advancements in compositing salts within porous matrices—such as silica,[24,25] zeolites,[26] MOFs,[27] hydrogels,[28,29] polymers,[30–32] and carbon materials[33]—have significantly improved their performance. Among these, the graphene aerogel is particularly notable for its ultra-high porosity (99.9%) and extremely low density (lower than 0.01 g cm^{-3}), allowing for salt loadings exceeding 90 wt%, double that of traditional porous materials.[33] Despite these advantages, the graphene aerogel still exhibits suboptimal mass transfer performance, primarily due to limited transport efficiency in bulk macrostructures. Additionally, the micro-sized pores within its open-porosity matrix fail to prevent leakage during overhydration. Furthermore, integrating bulk graphene aerogel structures into reactor designs poses challenges such as pressure drops or flow leakage through designated pathways.

In this work, we developed an advanced salt-in-matrix composite sorbent by encapsulating $CaCl_2$ within a micro- and macro-structured graphene aerogel sphere (GAS), specifically engineered for our proposed fast-charging/discharging e-thermal bank. The spherical particulate macrostructure not only minimizes pressure drop and enables high packing density but also enhances the availability of sorption sites and shortens diffusion pathways. The surface-oriented shell microstructure is designed to prevent sorbate leakage while allowing vapor transport for reversible sorption/desorption, and the aligned core channels facilitate improved intraparticle diffusion. Owing to this unique hierarchical architecture, the $CaCl_2$@GAS composite demonstrates a rapid sorption rate and a record-high sorption capacity of 3.96 g g^{-1}, resulting in an ultra-high energy density of 104 26 kJ kg^{-1} (based on dry sorbent mass). Thanks to the structural stability of both micro- and macro-architectures, this exceptional material performance is effectively translated to the prototype system with minimal performance loss. In an open system configuration, the e-thermal bank delivers an energy density of 7687 kJ kg^{-1} (based on initial dry sorbent mass) with a peak heating power of 2.96 kW kg^{-1}, and a cooling energy density of 1860 kJ kg^{-1} (based

on initial wet sorbent mass) with a peak cooling power of 3.016 kW kg^{-1}. Furthermore, the closed system configuration delivers an effective energy density of 1284 kJ kg^{-1} and a MW-to-thermal energy storage efficiency exceeding 77%.

Results and discussion

Fabrication and structural characterization of the $CaCl_2$@GAS sorbent

The fabrication of GAS is achieved through a simple and scalable wet-spinning approach. As illustrated in Fig. 1a, the process involves preparing graphene oxide (GO) ink, which is then extruded using a syringe pump into a coagulating bath. This is followed by hydrothermal reduction, directional freeze-drying, and salt loading to prepare the composite sorbent. The macrostructure of GAS is primarily influenced by the viscosity of the GO ink and the drop impact height, while the microstructure is governed by coagulation conditions and post-fabrication processing. The shape of the GO macrostructure evolves from doughnuts to discs, spheres, worms, and finally cylindrical fibres as the GO concentration increases from 2 to 25 mg mL^{-1}. Notably, variations in impact height distort the morphology, even at a fixed GO concentration. To achieve spherical structures—preferred for their fast kinetics and high packing density[34,35]—a GO concentration of 15–20 mg mL^{-1} is required, depending on impact height, GO flake dimensions, and functionalization density. However, preparing GO dispersions at such high concentrations poses challenges, necessitating an initial dilute dispersion followed by concentration *via* freeze-drying or evaporation. Additionally, higher GO concentrations result in structures with lower porosity and surface area compared to those fabricated with lower concentrations. A potential solution to achieve the desired ink viscosity while maintaining lower GO concentrations is the incorporation of dispersants such as silica, polymers, or divalent metal ions—an approach commonly used in GO-based additive manufacturing.[36] Among the various additives evaluated, we selected calcium chloride for its dual role: as an active component in the final composite and as a reducing agent during hydrothermal reduction. Its presence facilitated the successful fabrication of GAS at moderate graphene oxide (GO) concentrations (10–12 mg mL^{-1}) and an impact height of 3 cm. To produce spherical particles of varying sizes, GO ink with

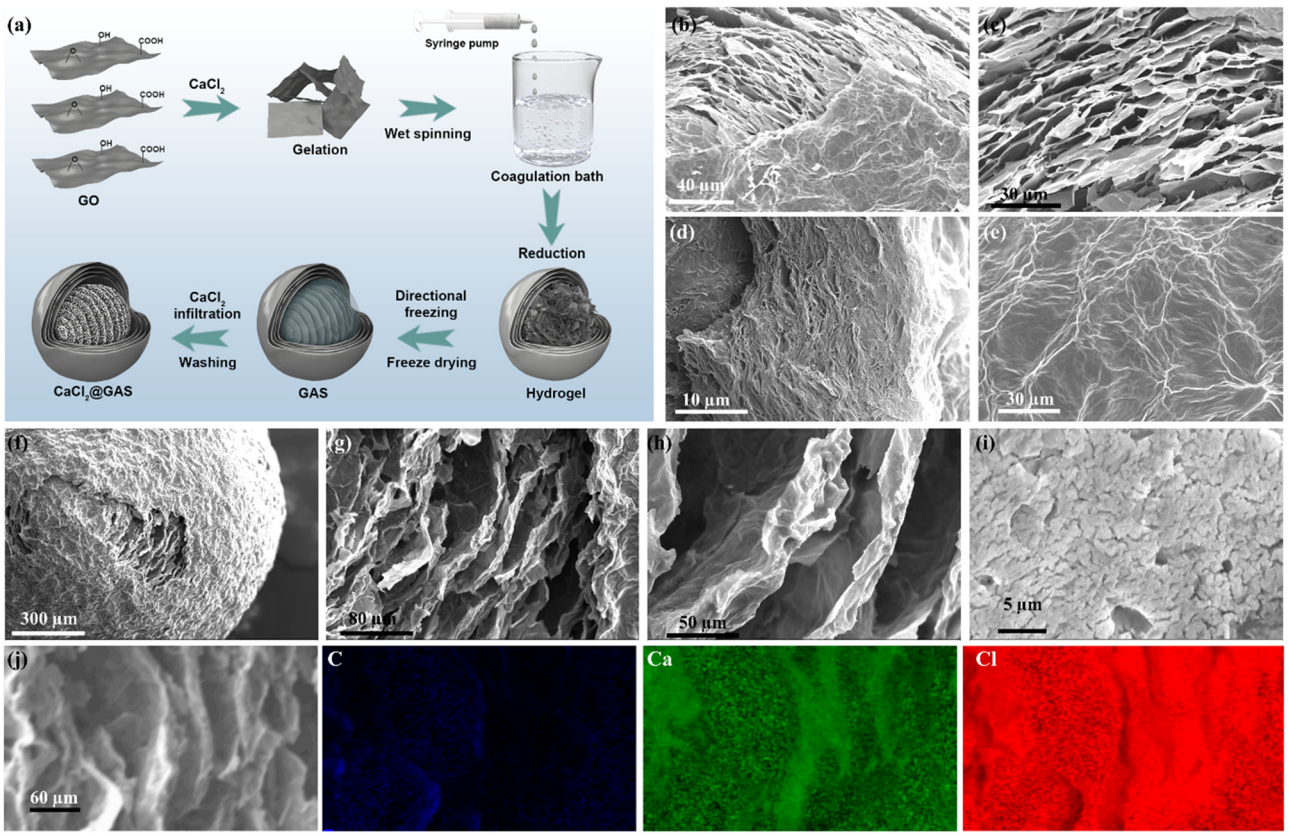

Fig. 1 Fabrication and morphological characterization of $CaCl_2$@GAS sorbent. (a) Schematic illustration of the material fabrication process. (b)–(e) SEM images of the empty GAS structure from different regions: (b) partially peeled-off skin revealing the core–shell architecture; (c) core region highlighting internal morphology; (d) cross-section of the shell displaying a densely packed yet porous structure; (e) top surface of the shell showing surface-aligned graphene sheets. (f)–(i) SEM images of the $CaCl_2$@GAS composite (with the skin removed) at varying magnifications: (f) low-magnification image showing both surface and internal features; (g) and (h) core region emphasizing the alignment of graphene sheets; (i) uniform decoration of $CaCl_2$ salt particles on the graphene surface. (j) SEM image of $CaCl_2$@GAS and corresponding elemental mapping.

optimized viscosity was extruded into a coagulation bath through a nozzle of required diameter. It is noteworthy that particle shape also depends on the extrusion speed, which can be adjusted to control particle size while keeping the ink concentration constant for other comparisons. The nozzle design can range from single-channel needles to multi-channel configurations (*e.g.*, shower nozzles) for large-scale production, demonstrating the practicality and scalability of this method.

As the GO droplet enters the coagulating bath, its core–shell microstructure evolves. Rapid curing of the spherical droplet occurs upon contact with the Ca^{2+} coagulating agent, driven by aggregation and phase segregation phenomena. The surface darkens as negatively charged GO sheets align parallel to the surface under electrostatic attraction from surrounding Ca^{2+} ions, forming a few μm thick dense outer shell (Fig. 1b–e). This parallel alignment alters pore size in the radial direction, narrowing pore size distribution to only nanopores. While surface sheets form a dense outer shell, interior sheets remain in the core due to restricted migration caused by high concentration. As a result, they are only partially aligned to each other in small domains due to interlamellar interaction, maintaining a less ordered structure.[37] During hydrothermal reduction, Ca^{2+} ions coordinate with the negatively charged GO sheets, indicating their role as a reducing agent (Fig. S2). During the freezing of the core–shell hydrogel spheres in liquid nitrogen-cooled hexane, the shell sheets remain surface-oriented due to rapid freezing, while the sheets in the core become fully aligned because of directional ice crystal growth (Fig. 1c). The surface-oriented shell acts as a barrier to liquid flow, slowing down salt solution infiltration during the salt loading process. To accelerate salt solution infiltration, we employed vacuum-assisted intrusion to force the salt solution into the core of the GAS structure. This was followed by repeated washing to remove salt from the surface and partially from the shell. Upon drying, salt particles uniformly deposited onto the graphene sheets, while the aligned microchannels remained open, even after salt loading (Fig. 1f–i). To further support the salt inclusion into the core, we removed the shell of $CaCl_2$@GAS composite particles and performed EDS mapping (Fig. 1j). The strong signals of Ca and Cl confirm the $CaCl_2$ deposition onto graphene sheets within the core of particles.

Thanks to its low density and high porosity, the GAS matrix can achieve salt loadings exceeding 90 wt%, depending on the concentration of the feed salt solution. To maximize sorption capacity while minimizing the risk of leakage, the optimal strategy is to use a saturated salt solution prepared at the operational RH relevant to the intended application.[38,39] For instance, in the practical scenario of our proposed e-thermal bank operating at 80–90% RH, this corresponds to a 15–22 wt% $CaCl_2$ solution at room temperature. Accordingly, we employed a 20 wt% $CaCl_2$ solution, which resulted in a final salt loading of 93 wt%. To examine the salt incorporation within GAS, we analysed the $CaCl_2$@GAS composite using X-ray tomography (XRT). Due to its extremely low density—approaching that of air—empty GAS could not be imaged *via* XRT. In contrast, reconstructed 2D and 3D images of the $CaCl_2$@GAS composite clearly show the formation of a dense, uniform outer shell and well-aligned microchannels in the core (Fig. 2a). These microchannels provide sufficient void space to accommodate the substantial volumetric expansion (~70 to 80%) that occurs during hydration (Fig. 2b). Consistent with SEM observations, 3D color-coded XRT reconstructions further reveal a uniform distribution of salt particles on the graphene sheets within the core (Fig. 2c). Visualization of the $CaCl_2$@GAS core using XRT confirms salt inclusion within the core, as empty GAS cannot be visualized by XRT. Furthermore, BET analysis demonstrates a high specific surface area of 150 $m^2\ g^{-1}$ for the empty GAS, along with a broad pore size distribution spanning microporous to macroporous regimes (Fig. 2d). Upon salt incorporation, both the surface area (reduced to 13 $m^2\ g^{-1}$) and total pore volume decrease, indicating successful loading of $CaCl_2$ into the GAS matrix.

Moreover, confined crystallization behaviours and temperature-driven dehydration were analysed using XRD (Fig. 2e). The near-identical diffraction patterns of pristine $CaCl_2$ and the $CaCl_2$@GAS composite indicate that the crystal structure of salt is preserved even after confinement within the nanopores of GAS. The significant reduction in the intensity of the graphitic peak at $2\theta \approx 26^\circ$ in the composite compared to pristine GAS reflects the high salt content, with salt crystal peaks dominating the XRD pattern of $CaCl_2$@GAS. Temperature-dependent XRD analysis further elucidated the multistep desorption behaviour of the composite sorbent (Fig. 2f). At 25 °C, the $CaCl_2$ exists predominantly in solution form, leading to minimal crystalline diffraction. As the temperature increases to 60 °C, $CaCl_2{\cdot}4H_2O$ begins to crystallize due to progressive water evaporation. It is noteworthy that $CaCl_2{\cdot}6H_2O$ is not detected, as it melts at approximately 30 °C and does not form a stable crystalline phase under these conditions. Upon further heating to 80–100 °C, $CaCl_2{\cdot}4H_2O$ undergoes stepwise dehydration, transforming into $CaCl_2{\cdot}2H_2O$. This intermediate phase continues to dehydrate into $CaCl_2{\cdot}H_2O$ at 120 °C and finally reaches the anhydrous $CaCl_2$ form at 150 °C.[33] During hydration, gaseous water can reversibly react with the encapsulated salt, completing the reversible sorption–desorption cycle. As previously discussed in the SEM and XRT analyses and illustrated in Fig. 3a, our surface-engineered core–shell microstructure effectively retains the liquid within the core, significantly reducing leakage risk—unlike typical open-porosity structural materials, which often experience leakage during overhydration.

Water sorption–desorption dynamics and corresponding enthalpy evaluation

We assessed the sorption and desorption performance of the developed composite sorbent using a dynamic vapor sorption (DVS) analyzer. Compared to pristine $CaCl_2$, the monolithic composite sorbent demonstrated significantly faster water sorption under identical conditions. This enhancement is attributed to the dispersion of fine salt crystals within a hierarchically porous matrix. However, the improvement is partially limited by the reduced exposure of sorption sites

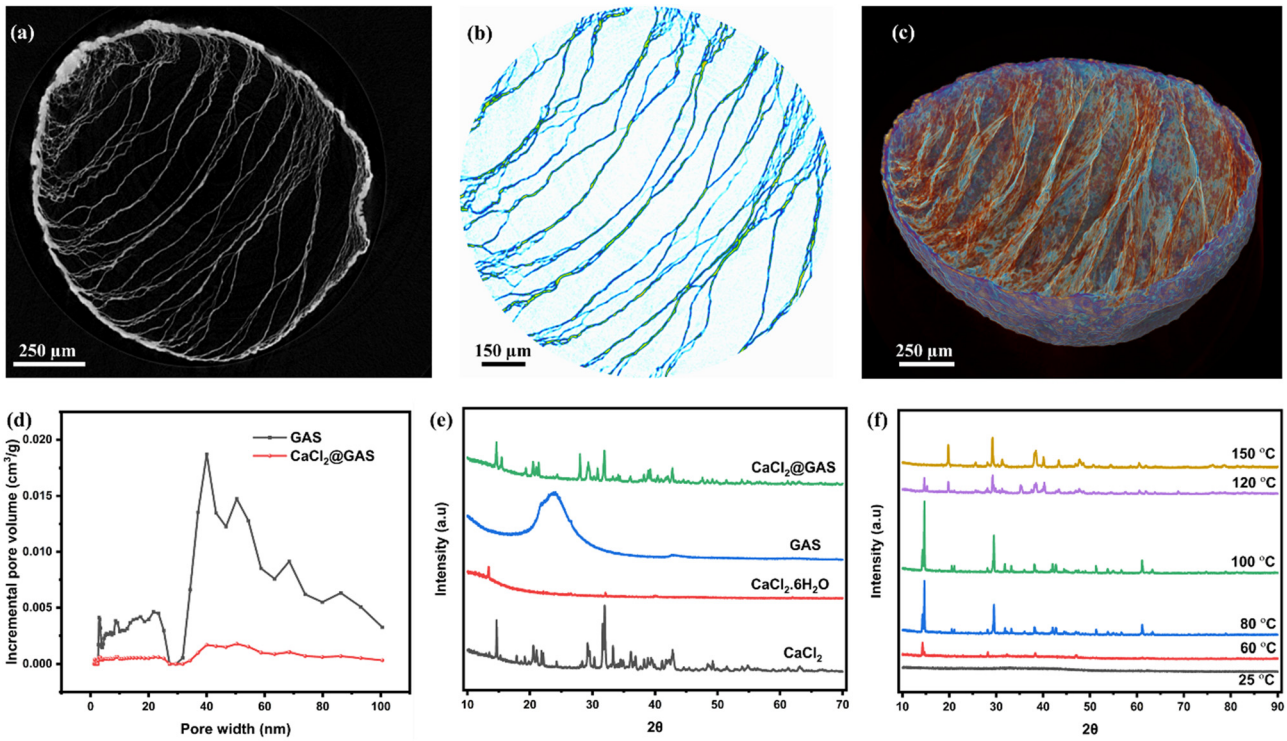

Fig. 2 Structural characterization of the $CaCl_2$@GAS sorbent. (a) Reconstructed 2D image of $CaCl_2$@GAS showing the core–shell microstructure. (b) Reconstructed 2D image of the $CaCl_2$@GAS core alone, revealing internally aligned channels. (c) 3D tomographic slice of $CaCl_2$@GAS confirming the spatial distribution of salt particles within the GAS matrix. (d) BET pore size distribution curves for the empty GAS and $CaCl_2$@GAS composite. (e) XRD patterns of $CaCl_2$, $CaCl_2{\cdot}6H_2O$, GAS, and $CaCl_2$@GAS. (f) Temperature-dependent XRD patterns of $CaCl_2$@GAS. The X-ray source is Cu Kα radiation and unit of 2θ is degrees.

within the macrostructure. To address this limitation, our fabrication strategy utilized small spherical particles, which minimized diffusion distances and increased the exposure of sorption sites. This approach substantially improved sorption kinetics relative to both pristine $CaCl_2$ and the monolithic composite (Fig. 3b). The enhanced uptake capacity and sorption rate result from high salt loading and the open porosity of the matrix, further supported by aligned channels (Fig. S3). Desorption kinetics were evaluated using a moisture analyzer capable of analyzing gram-scale samples. Under identical conditions, the $CaCl_2$@GAS composite exhibited faster desorption kinetics than its monolithic counterpart (Fig. S4). Notably, sorption kinetics increase with decreasing particle size due to the enhanced sorption sites (Fig. 3c). Balancing sorption rate and pressure drop at the reactor level, we selected an optimal particle size of 1.2 mm for further studies.

Additionally, sorption capacity (Fig. 3d) and sorption rate (Fig. S5) both increased with RH, ranging from 30% to 90%. It is important to note that the sorption mechanism shifts from gas-phase chemisorption at low RH to liquid-phase absorption at high RH (Fig. 3e). At 90% RH, the $CaCl_2$@GAS composite achieved a maximum water uptake of 3.96 g g^{-1}, surpassing that of previously reported $CaCl_2$ composites and approaching the performance of leading hydrogels while maintaining superior sorption kinetics (Table S1). The absorbed water could be desorbed through either temperature swing (*via* heating; Fig. S4) or pressure swing (*via* reduced vapour pressure; Fig. S6). As expected, thermally driven desorption was faster due to lower energy barriers, while pressure-driven desorption highlights the material's potential for evaporative cooling applications. We also evaluated the energy storage capacity and cyclability of the $CaCl_2$@GAS composite using vapor-coupled simultaneous thermal analysis (STA). At 60% RH, the composite achieved a water uptake capacity of 1.93 g g^{-1}, corresponding to an energy density of 4987 kJ kg^{-1} based on its dry weight (Fig. 3f). Compared to DVS results, slightly higher uptake was observed in STA measurements, likely due to instrument-specific differences or condensation issues (Fig. 3g). When tested at 90% RH, the energy density further increased to 10 426 kJ kg^{-1}— outperforming previously reported salt-based composite sorbent materials (Fig. 3h and Table S1). Moreover, consistent water uptake over three consecutive sorption–desorption cycles confirms repeatability of the results (Fig. 3i). In summary, the $CaCl_2$@GAS composite demonstrates exceptional water uptake, rapid (de)sorption kinetics, and ultra-high energy density, confirming its strong potential for use in advanced TCS systems.

Prototype performance of the closed cycle e-thermal bank

To evaluate the prototype performance of our proposed e-thermal bank, the developed $CaCl_2$@GAS sorbent was integrated into a vacuum TCS system, as illustrated in Fig. 4a.

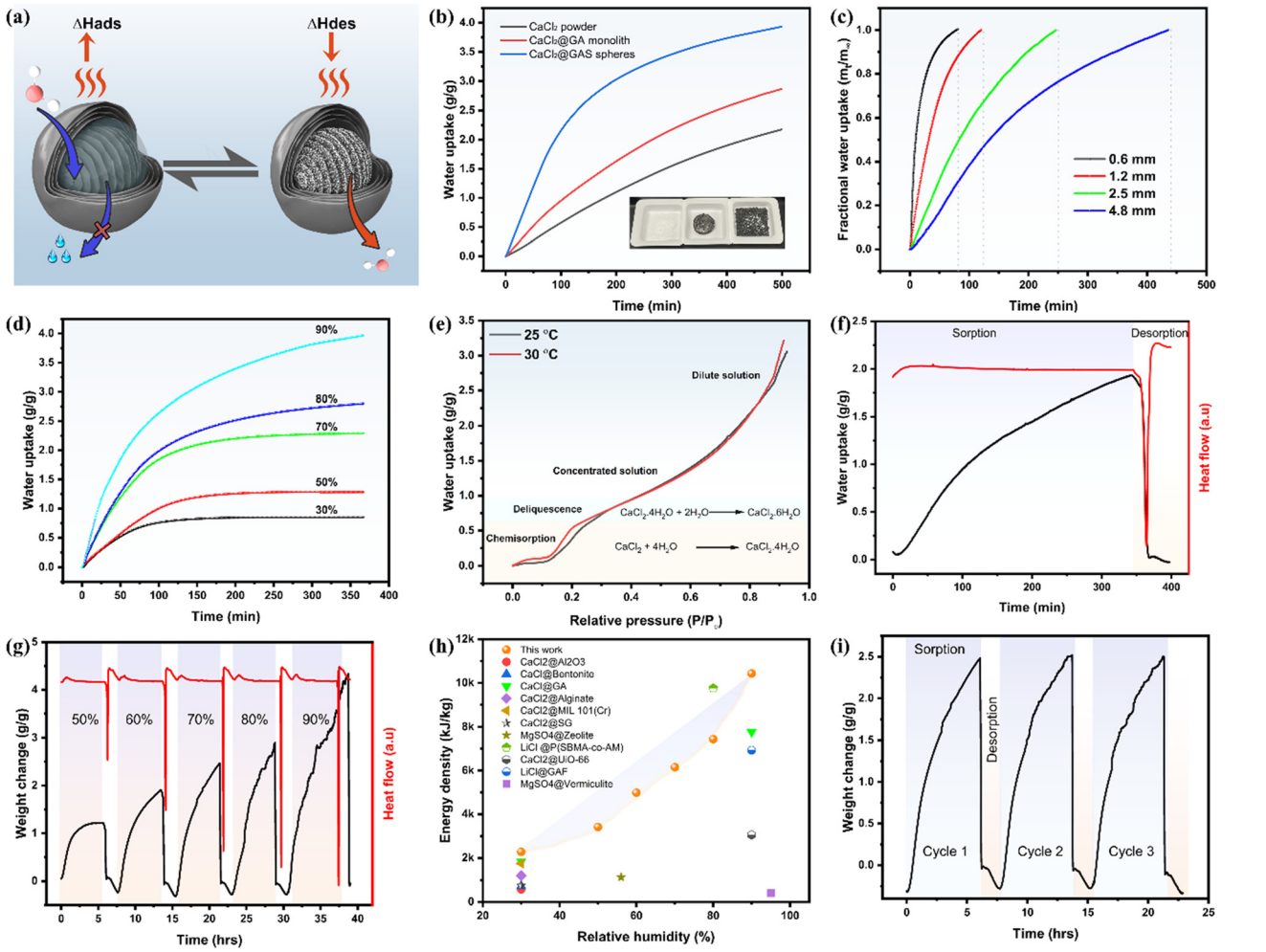

Fig. 3 Water sorption–desorption dynamics and corresponding enthalpy evaluation. (a) Schematic illustration of the reversible sorption/desorption process and the mechanism of leakage prevention. (b) Water sorption isotherms of pure $CaCl_2$, $CaCl_2$@GA, and $CaCl_2$@GAS under identical conditions. (c) Effect of particle size on fractional water uptake at 80% RH. (d) Water sorption isotherms of 1.2 mm $CaCl_2$@GAS spheres measured at different fixed relative humidities. (e) Sorption isotherms of 1.2 mm $CaCl_2$@GAS under varying water vapor partial pressures. (f) Water sorption–desorption curve and corresponding DSC signal, showing sorption at 25 °C and 60% RH, followed by desorption at 130 °C. (g) Water sorption–desorption curves and corresponding DSC signals at increasing RH. (h) Energy density of $CaCl_2$@GAS as a function of RH, compared with other reported salt-based composite sorbents (detailed comparison in Table S1). (i) Sorption–desorption cyclability of $CaCl_2$@GAS over three consecutive cycles: sorption at 70% RH and desorption at 130 °C.

During the discharging phase, the sorbate evaporates from the evaporator and reacts with the $CaCl_2$@GAS sorbent material, generating cooling at the evaporator and heating at the reactor. The generated heat is extracted *via* airflow through the coiled inner tube of the reactor. In the charging phase, thermal energy is supplied to drive desorption, and the released vapours condense in the condenser, releasing condensation heat. The resulting liquid then returns to the evaporator to initiate the next cycle. In this process, the reaction and condensation enthalpies are harnessed for heating, while the evaporation enthalpy can be utilized for cooling applications. This dual functionality of providing both heating and cooling highlights the potential for integrating the e-thermal bank with BTM, thereby enhancing overall energy efficiency through the chemical heat pump effect. While BTM integration has already been demonstrated in our previous work and by others, the present study primarily focuses on evaluating the system's capability for cabin heating and cooling.

Unlike previous studies that primarily report key performance metrics derived from water sorption isotherms, our work experimentally demonstrates prototype performance under realistic operating conditions.[40,41] Both pure water and an ammonia–water solution were considered as potential sorbate candidates, and their performance was assessed in terms of temperature lift, energy density, and response time to meet the operational requirements of the proposed e-thermal bank. Although we did not characterize ammonia uptake by our developed sorbent due to instrumental constraints, prior studies confirm the feasibility of the ammonia–$CaCl_2$ reaction, which offers the added benefit of a purely gas–solid sorption.[42,43] Unlike water condensation, ammonia exhibits a strong affinity for water, leading to direct absorption by the

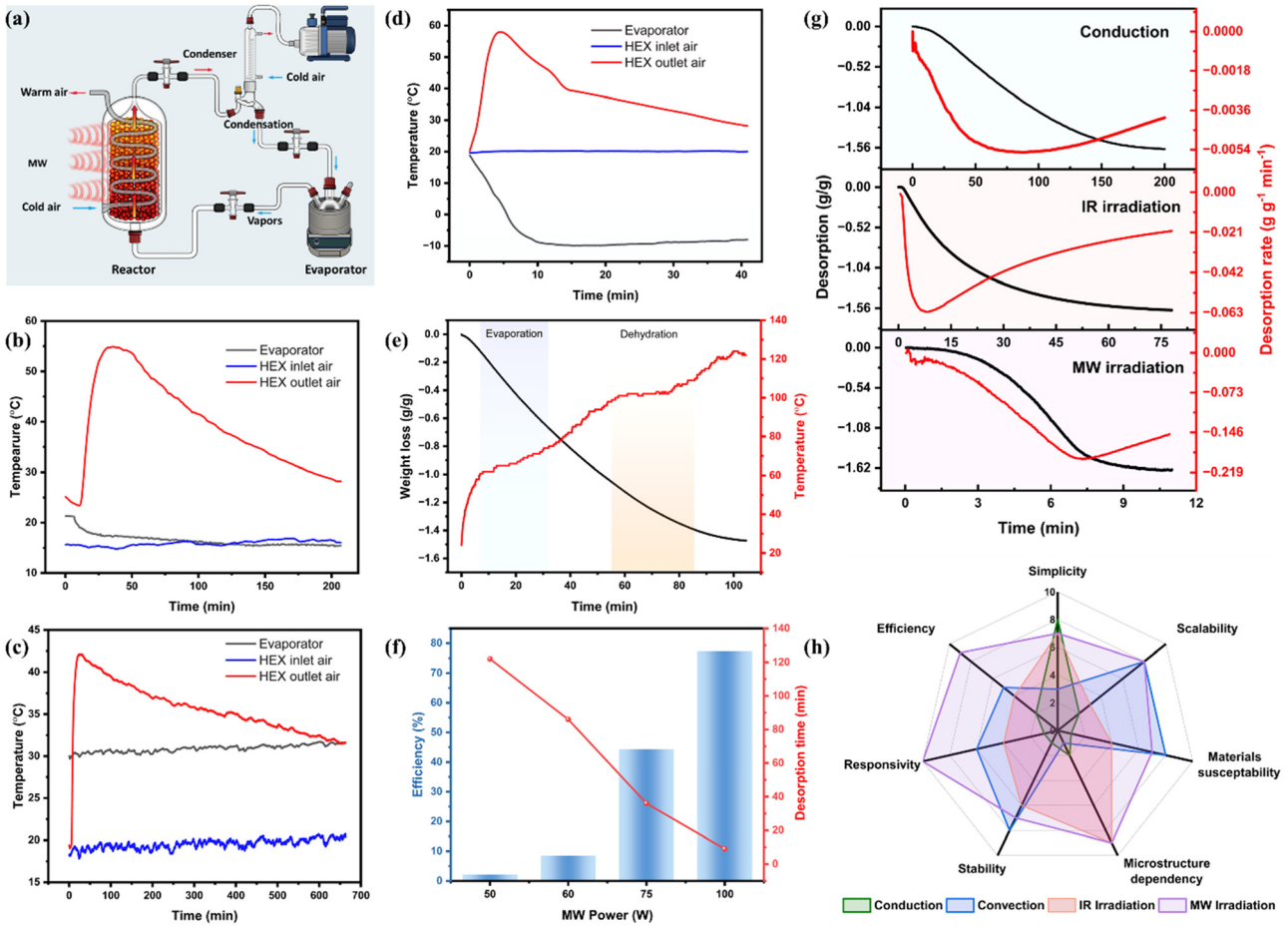

Fig. 4 Prototype performance of the closed-cycle e-thermal bank. (a) Schematic illustration of the prototype TCS system operation. During charging, MW heating raises the temperature of the sorbent bed, driving desorption and generating water vapour. The released vapour is then condensed in the condenser, and the condensed water returns to the evaporator. During discharging, water evaporates from the evaporator under low pressure and flows to the sorbent bed, where it is adsorbed by the sorbent, releasing heat. The generated heat is removed through the glass heat exchanger and carried away by the airflow. (b) Discharging performance using a 25% v/v ammonia–water solution as the sorbate with 5 L min^{-1} airflow through the heat exchanger. (c) Discharging performance using pure water as the sorbate under identical airflow conditions. (d) Temperature drop at the vacuum-insulated evaporator with 25% v/v ammonia–water solution. Note: the temperature lift at the reactor is shown for reference only, as it typically represents waste heat in conventional cooling applications. (e) Time–temperature–weight loss evolution during 60 W MW heating. (f) Effect of MW power on charging time and MW-to-TCS energy storage efficiency. (g) Comparison of desorption performance under conduction, IR, and MW heating. (h) Comparative evaluation of conduction, convection, IR radiation, and MW irradiation for thermal charging in TCS applications.

liquid phase. This process releases sorption enthalpy at the evaporator during charging and eliminates the need for a condenser. Under realistic winter conditions, when the evaporator temperature falls below 20 °C, water fails to generate sufficient vapor pressure to produce a temperature lift at the reactor level. In contrast, a 25% v/v ammonia–water solution achieves a peak temperature lift of approximately 8 °C (Fig. S7a). This indicates superior performance of the ammonia–water solution over pure water. However, as evaporator temperature decreases, vapor pressure drops, thereby limiting the achievable temperature lift. To compensate, either the system pressure must be significantly reduced to enable low-temperature evaporation, or the evaporator temperature must be increased to boost vapor pressure. Our innovative design addresses this challenge by utilizing battery waste heat to preheat the evaporator, thereby maintaining a stable evaporator temperature and ensuring sufficient vapor pressure. By maintaining the evaporator at ~20 °C, the outlet air temperature can reach up to 35 °C, with a peak temperature lift of 17 °C (Fig. S7b). Despite this improvement, the achieved temperature lift remains insufficient for typical cabin heating applications, which generally require outlet air temperatures above 35 °C. While we did not monitor the sorbent material temperature due to design limitations, it is expected to exceed the outlet air temperature.

To simultaneously achieve rapid response and sufficient temperature lift, we examined the combined effect of preheating the evaporator using recovered battery heat and lowering the system pressure *via* a moderate vacuum (0–30 kPa). This facilitates rapid evaporation and directs vapor flow through the reactor. Using a 25% v/v ammonia–water solution, maintaining the evaporator at 20 °C and applying a 10 kPa vacuum, the

system achieved a temperature lift of 37 °C and an outlet air temperature exceeding 55 °C at a 5 L min^{-1} airflow rate (Fig. 4b). At a cut-off temperature of 30 °C, the system demonstrated an effective energy density of 987 kJ kg^{-1} based on dry $CaCl_2$@GAS mass only. It is important to note that the reported energy density reflects effective energy delivered above the 30 °C threshold; the actual energy density is higher, as the outlet air temperature remains elevated above the inlet. Due to the lower vapor pressure of pure water compared to ammonia–water solutions, achieving adequate temperature lift requires higher evaporator temperatures and vacuum pressures. By maintaining the evaporator at 30 °C and applying a vacuum pressure of 40 kPa, the system achieved a temperature lift of 27 °C, a peak outlet air temperature of 45 °C, and an energy density of 1284 kJ kg^{-1} (Fig. 4c). The higher energy density observed with pure water as a sorbate, relative to ammonia–water, is attributed to two main factors: (1) the hydration reaction is more exothermic than ammoniation, and (2) the higher evaporator temperature in the pure water case contributes additional energy through condensation heat transfer. This indicates that recovering waste heat not only stabilizes evaporator temperature but also amplifies heat output through a thermal gain effect. Conversely, in cooling applications without evaporator preheating, pure water achieves a temperature drop of 11 °C (Fig. S8), while the ammonia–water solution can deliver a 30 °C temperature drop, reaching as low as −10 °C (Fig. 4d). This temperature drop at the evaporator is highly dependent on the amount of evaporative liquid and is therefore not strictly quantitative; however, it highlights the strong potential of the proposed e-thermal bank for cooling applications.

For the thermal charging of the e-thermal bank, we demonstrated a microwave (MW) heating approach that is not only simple and scalable, but also commercially viable.[44] The radiative nature of MW energy delivery, along with its ability to selectively heat polar sorbate molecules such as water and ammonia, and its deep penetration capability, collectively enhance both desorption kinetics and overall energy efficiency. These advantages make the conversion of electrical energy to MW power worthwhile, despite some conversion losses. To evaluate MW-powered thermal charging of the proposed e-thermal bank, we conducted the second half of the experiment using water as the sorbate under ambient conditions, rather than a closed-loop setup. This was done to specifically examine the effect of MW irradiation on the sorbent's temperature, mass change behaviour, and more importantly energy conversion and storage efficiency. A flexi-wave MW generator, integrated with a weight balance and an infrared (IR) temperature sensor, was employed to monitor real-time mass loss and temperature evolution during MW exposure (Fig. S9). This system allows operation in either fixed MW power mode or temperature-controlled mode. To study the impact of MW power on the temperature response of the sorbent, we initially operated the system in fixed-power mode. As expected, anhydrous $CaCl_2$—due to its low dielectric constant—did not absorb MW energy, and no increase in temperature was observed during 50 W MW irradiation (Fig. S10). Surprisingly, neither the dihydrate nor the hexahydrate forms showed any significant temperature rise, indicating that they do not absorb MW energy effectively. These results suggest that only free or loosely bound water molecules can respond to MW radiation. In contrast, tightly bound water such as crystalline water where water molecules are coordinated to metal cations, does not respond effectively to MW energy, especially at low MW power. The temperature rise of melted hexahydrate during MW irradiation further validates our conclusion (Fig. S11).

The lack of MW absorption by anhydrous $CaCl_2$ provides a key advantage during MW-driven desorption, as it prevents unnecessary heating once desorption is complete. However, the poor MW absorption of $CaCl_2$ dihydrate presents a challenge, potentially leading to incomplete dehydration. To overcome this limitation, we leveraged the exceptional MW-to-thermal energy conversion capability of graphene—enabled through conduction losses—in our $CaCl_2$@GAS composite. This design ensures complete dehydration, even when the dihydrate phase becomes MW-inactive. To quantify this effect, the $CaCl_2$@GAS sorbent was initially hydrated at 60% RH and subsequently subjected to MW-driven dehydration at varying MW power levels ranging from 50 W to 100 W. At 50 W MW power, the sorbent temperature increased to nearly 100 °C, which enabled the desorption of most of the physically sorbed water (Fig. S12a). However, full dehydration was not achieved, as the decomposition temperature of $CaCl_2{\cdot}2H_2O$ exceeds 100 °C. To further investigate the influence of MW power on the dehydration process, the MW input was increased to 60 W under otherwise identical sorbent mass and other conditions. As shown in the mass change and temperature evolution curves, the sorbent initially undergoes a rapid temperature rise to 65 °C due to sensible heating, with no significant mass loss observed during this phase (Fig. 4e). This is followed by a plateau, where the input MW energy is primarily utilized for the evaporation of liquid water. Once most of the liquid water is removed and the dihydrate phase forms, the temperature begins to rise again. A second plateau is observed at elevated temperatures, corresponding to the dehydration of the dihydrate phase. Finally, the temperature increases further and stabilizes due to balance between thermal conversion and ambient heat losses, marking the completion of the desorption process. This progression is corroborated by the stabilization of the mass loss curve, confirming complete dehydration of the sorbent.

Further, increasing the MW power to 75 W and 100 W, the desorption time can be reduced from more than hour to just a few minutes (Fig. S12b and c). This rapid chargeability highlights the suitability of our proposed MW-based charging approach not only for conventional EVs but also for fast-charging EV applications. Moreover, increasing MW power not only shortens the desorption time but also enhances the MW-to-thermal energy storage efficiency, calculated using the input–output energy balance equation: $\eta = (m{\cdot}\Delta H)/(P{\cdot}t)$, where m is the mass of the sorbent, ΔH is the desorption enthalpy measured using STA, P is the applied MW power, and t is the desorption duration (Fig. 4f). At 100 W MW power, the MW-to-thermal energy storage efficiency reaches up to 77%, underscoring the effectiveness of this volumetric heating approach.

The high energy conversion efficiency at elevated power levels is primarily attributed to minimized heat losses during the significantly shortened charging period. To further demonstrate the superiority of MW heating over conventional conduction, convection, and infrared (IR) radiation methods, we performed desorption experiments under a fixed-temperature mode that mimicked these other heating mechanisms. For IR-driven desorption, we employed a TA moisture analyser, while for conduction-driven desorption, we used a laboratory oven integrated with a balance. In all three methods, the desorption temperature was fixed at 120 °C. For IR and MW heating, an identical ramp rate was used to reach 120 °C, while conduction heating was initiated by directly placing the sample at the target temperature. Under these controlled conditions, MW heating achieved a desorption rate three times higher than IR and 36 times higher than conduction (Fig. 4g). Complete desorption was achieved in approximately 8 minutes using MW, compared to 50 minutes with IR and 125 minutes with conduction heating. This performance difference underscores the superiority of MW heating, owing to its localized and deep penetration nature. Although the experiments were performed under matched conditions, the inherently different heating mechanisms make direct quantification challenging; thus, the results serve to illustrate performance trends rather than absolute comparisons. Furthermore, the MW-based charging approach is not only fast and energy-efficient but also stable due to its uniform heating profile. It is compatible with a wide range of materials and less sensitive to the microstructural variations of the sorbent (Fig. 4h). These advantages give MW heating a significant edge over other methods, which often require strict material properties and specialized system designs.

Prototype performance of the open cycle e-thermal bank

In addition to the closed system investigation, the developed $CaCl_2$@GAS composite sorbent was also evaluated for open system applications, as illustrated in Fig. 5a. During MW-driven charging, the sorbent material was directly irradiated with MW energy while cold air was simultaneously passed through the material. Unlike conventional open systems—also shown in Fig. 5a—which suffer from significant heat losses due to the use of separate electric heaters and convective heat transfer, our proposed design minimizes such losses by directly irradiating the sorbent, thereby improving thermal efficiency. As the MW irradiation proceeds, the temperature of the sorbent increases, triggering desorption and releasing water vapor, which is carried away by the airflow. As depicted in Fig. 5b, both the outlet air temperature and humidity ratio rise during irradiation, confirming ongoing desorption. Upon reaching a peak, the humidity ratio gradually declines and eventually stabilize, indicating near completion of the desorption process. It is worth noting that residual humidity in the outlet stream, even after desorption is complete, may result from moisture condensation within the extended reactor tube. Importantly, the warm outlet air produced during this charging process—typically in the range of 30–70 °C—can be effectively utilized for pre-conditioning EV battery packs *via* a heat exchanger, as batteries require elevated temperatures during fast-charging operations.[45]

During the discharging process of the open-system e-thermal bank, humid cold air is passed through the fully charged (dehydrated) sorbent bed, where the exothermic hydration of the sorbent generates heat. This heat is transferred to the passing airflow, producing a stream of warm, dry air suitable for cabin heating. The resulting temperature lift is highly dependent on the water content (humidity ratio) of the inlet air. When ambient air has sufficient humidity (typically 75–85% RH), it can be directly passed through the sorbent bed to yield warm outlet air. In cases of low ambient humidity, the air can be pre-humidified by bubbling through a water tank prior to contact with the sorbent material, as illustrated in Fig. 5a. When inlet air at 18 °C and 80% RH (corresponding to a humidity ratio of 14 g H_2O/kg dry air) was passed through the $CaCl_2$@GAS sorbent, the outlet humidity decreased and temperature rose to 37 °C, yielding a temperature lift of 19 °C (Fig. 5c). To evaluate the spatial progression of the discharging process, thermocouples were strategically placed at different positions within the sorbent bed. TCM T1, located near the air inlet at the bottom, and TCM T2, positioned at the midsection of the bed, revealed a sequential, layer-by-layer hydration process: the bottom layer (near T1) exhibited a temperature rise first, followed by a decline as hydration completed, while the mid-layer (T2) subsequently underwent the same thermal transition. Additionally, the temperature measured near the reactor wall at the top layer (TCM T3) indicates the absence of air leakage along the reactor walls. This observation confirms the uniform mass transfer throughout the packed bed of mm-sized $CaCl_2$@GAS sorbent particles. Moreover, the humidity difference between inlet air and outlet air reveals water sorption during the discharging process (Fig. 5c). The outlet humidity profile, consistent with DVS results, reveals a characteristic two-step sorption mechanism: an initial gas–solid sorption, during which the outlet humidity stabilizes around 5 g kg^{-1}, followed by a gas–liquid sorption phase where the outlet humidity increases beyond 8 g kg^{-1}.

Furthermore, the warm outlet air generated for cabin heating can be recirculated through a water tank to restore its humidity before being reintroduced into the sorbent bed for subsequent cycles. This recirculation strategy minimizes thermal losses while enhancing thermal output, as warm air at a fixed RH holds more water vapor than cold air, thereby improving the overall efficiency of the heating process. This enhancement is supported by experimental results showing that increasing the inlet air temperature to 25 °C at 80% RH leads to a higher sorbent bed temperature compared to 18 °C inlet air under the same RH conditions (Fig. S13a). A further increase in inlet air temperature to 30 °C results in a peak sorbent bed temperature approaching 100 °C and an outlet air temperature of 52 °C—yielding a 22 °C temperature lift (Fig. S13b), which is sufficient to maintain a comfortable cabin environment even under freezing outdoor conditions, while also allowing for ventilation by mixing with 30% ambient cold air. To calculate the energy density, we selected the experiment with a higher

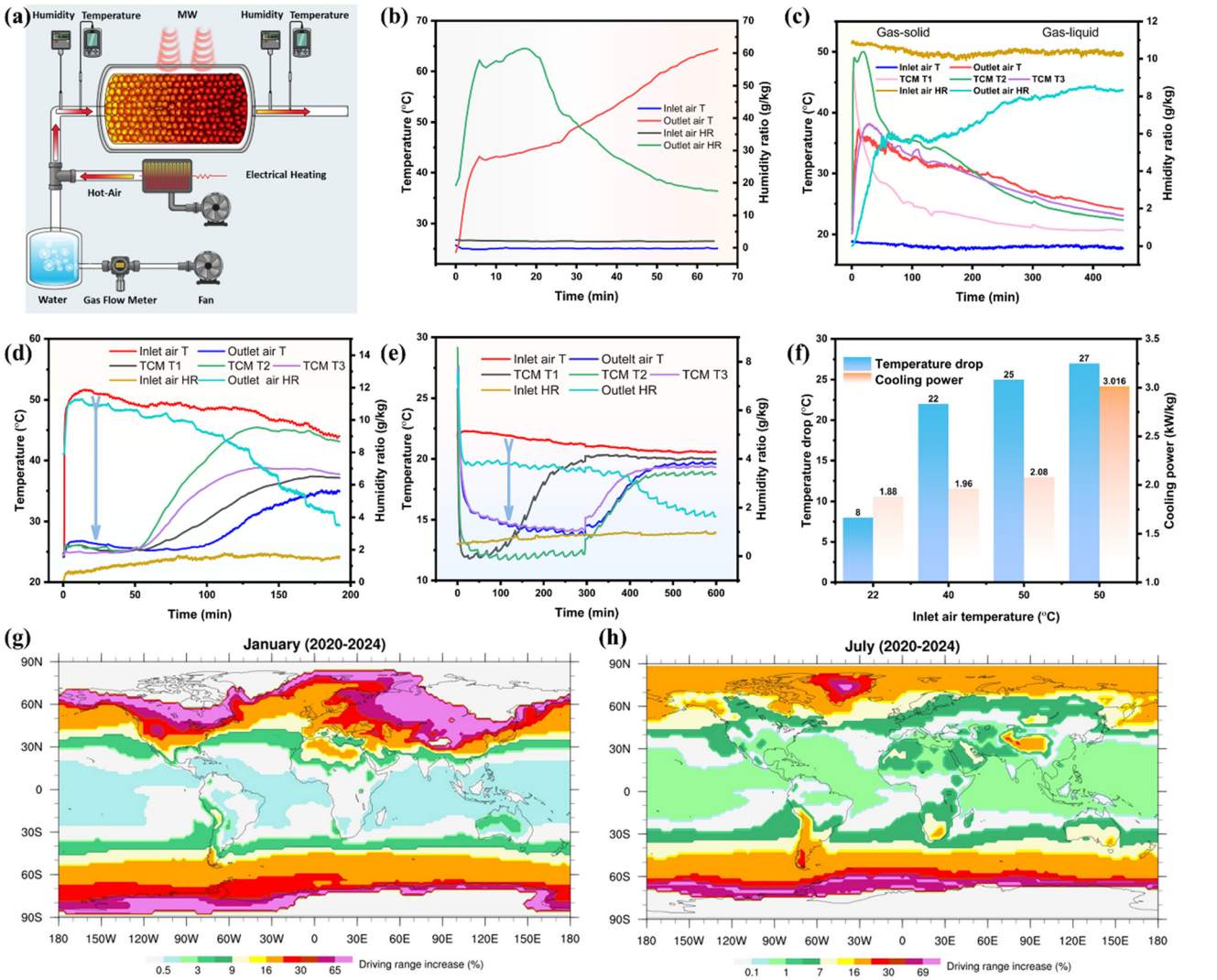

Fig. 5 Prototype performance of the open-cycle e-thermal bank. (a) Schematic illustration of the prototype open-system operation. During charging, MW heating raises the temperature of the sorbent bed and drives water desorption. The desorbed water vapour is carried away by the cold inlet airflow, producing a warm, humid (wet) outlet stream. During discharging, cold air is bubbled through a water tank to reach a controlled humidity level and then passed through the sorbent bed, where water vapour is absorbed by the sorbent, releasing heat. The heat is carried away by the airflow, resulting in a hot, dry outlet stream. (b) Temperature and humidity evolution during charging under 150 W MW power and a flow rate of 30 SL min^{-1}. (c) Temperature and humidity evolution during discharging at a flow rate of 20 SL min^{-1}. (d) Temperature and humidity evolution during evaporative cooling at 20 SL min^{-1} with an inlet air temperature of approximately 50 °C. (e) Temperature and humidity evolution during evaporative cooling at 20 SL min^{-1} with an inlet air temperature of approximately 22 °C. (f) Temperature drop and cooling power as a function of inlet air temperature. (g) Calculated colour map showing the percentage increase in EV driving range due to e-thermal bank integration during winter, across the globe. (h) Calculated colour map showing the percentage increase in EV driving range due to e-thermal bank integration during summer, across the globe.

inlet air temperature (30 °C), thereby reducing the influence of ambient heat on the calculation. Based on dry $CaCl_2$@GAS mass, the specific energy density was calculated to be approximately 7687 kJ kg^{-1} (equivalent to 2135 Wh kg^{-1}), with a peak power density of 2.96 kW kg^{-1}. These reported energy density and power density values not only surpass all previously reported TCS systems but also exceed the energy density of commercial lithium-ion batteries by a factor of 7 and even outperform the U.S. Department of Energy's targets for next-generation thermal energy storage technologies.[19] Moreover, the continuous supply of warm, dry air not only supports passenger comfort but is also highly effective for demisting windows—eliminating the need for energy-intensive demisting processes and contributing to enhanced driver safety during winter conditions.

For the cooling mode of the open-cycle e-thermal bank, two reactor configurations were investigated based on the evaporative cooling concept.[46–48] In the proposed design, during discharging, ambient air is first passed through a drying sorbent (fully dehydrated) bed, where it becomes warm and dry. This air is then cooled to near-ambient temperature *via* a heat exchanger before being directed through a wet sorbent bed (fully hydrated), where evaporative cooling occurs—producing a stream of cool, humidified air suitable for cabin cooling.

During the charging process, the drying reactor is regenerated using MW energy input (as presented in Fig. 5b), producing warm, humid air. This humid air after cooling down can optionally pass through the evaporative cooling reactor to replenish moisture levels, particularly in cases where ambient RH is insufficient. Due to the strong hygroscopic nature of the $CaCl_2$@GAS sorbent, it effectively absorbs water vapor even at low RH, as confirmed by DVS sorption measurements. Additionally, more than 95% of the absorbed water can be desorbed by simply passing dry air though it at 25 °C, underscoring its suitability for evaporative cooling applications (Figure S6). In this study, $CaCl_2$@GAS was utilized in both the drying and evaporative cooling reactors; however, employing distinct salts —such as $CaCl_2$ for drying and LiCl for evaporative cooling—could further enhance performance. It is important to note that, while only the results of the evaporative cooling reactor are presented here, the drying behaviour closely mirrors that observed in the open-system heating mode.

As shown in Fig. 5d, when dry air at 50 °C was passed through a wet $CaCl_2$@GAS sorbent bed (preconditioned at 60% RH), the outlet air humidity ratio increased to 10 g kg^{-1} and the temperature dropped to 25 °C—demonstrating the strong cooling effectiveness of the system. Based on the temperature difference between the inlet and outlet air, and the wet weight of the sorbent material, the calculated cooling energy density is 1860 kJ kg^{-1} (516 Wh kg^{-1}). In real-world summer conditions, where ambient temperatures typically range from 40 to 45 °C in many regions, the system was able to reduce the outlet air temperature to approximately 20 °C, corresponding to a temperature drop of about 22 °C (Fig. S14). For effective cooling applications, air temperatures below 20 °C are generally desirable. To achieve this, an air recirculation strategy—similar to the approach used in heating applications—can be employed. For instance, ambient air at 45 °C can first be cooled to 22 °C. After drying, this pre-cooled air can be recirculated through a wet sorbent bed, further reducing the temperature to around 14 °C, as presented in Fig. 5e. Both temperature drop and cooling power increase with rising inlet air temperature, reaching a maximum temperature drop of 25 °C and a cooling power of 2.08 kW kg^{-1} at an inlet temperature of 50 °C (Fig. 5f). Moreover, increasing the airflow rate from 20 SL min^{-1} to 30 SL min^{-1} at nearly the same inlet air temperature (~50 °C) resulted in a higher cooling power of 3.016 kW kg^{-1}, highlighting the system's adaptability for fast-response cooling under varying operational conditions (Fig. 5f and Fig. S15).

To assess how integrating an e-thermal bank could improve EV performance in thermally challenging environments, we analysed real-world driving data comprising 345 622 trips from 300 EVs owned by 278 customers of the Salt River Project.[1] The dataset shows that maximum driving range occurs within an ambient temperature window of 21–25 °C (Table S2), where battery energy efficiency is the highest and cabin HVAC demand is minimal; this range is therefore taken as the 100% baseline.[49] When ambient temperatures move away from this optimum—particularly under cold conditions—the driving range decreases markedly.[50] In this context, the proposed e-thermal bank, if capable of fully supplying onboard HVAC demand with minimal energy consumption while maintaining the battery within its optimal temperature window (and with an added mass comparable to modern vapour-compression HVAC systems or heat pumps), could substantially mitigate climate-induced range losses. To quantify the potential benefit at the global scale, we analysed average ambient temperature data for January and July (2020–2024), representing typical winter and summer conditions, respectively (Fig. 5g, h and Fig. S16). The resulting colour maps indicate that the e-thermal bank could improve driving range across diverse climate zones. In colder regions—including Canada, Russia, and parts of Europe—substantial range extensions are projected during winter months. Likewise, regions exposed to extreme summer temperatures, such as the southwestern United States, parts of Africa and South Asia, the Middle East, and Australia, are expected to gain improved range performance during hot periods. Overall, these results suggest a potential driving-range extension of ~30% in winter and ~20% in summer for average temperature scenarios across most of the world. Notably, these values represent an upper-bound estimate, based on the assumption that the e-thermal bank fully covers HVAC loads over the driving cycle.

Importantly, the overall mass/volume footprint of the proposed e-thermal bank is expected to be comparable to, or potentially lower than, conventional vapour-compression air-conditioning systems or heat-pump modules used in modern EVs, since it partially replaces continuous electrical heating/cooling with stored thermochemical energy. Owing to the ultra-high gravimetric energy density of the $CaCl_2$@GAS sorbent and the efficient thermochemical storage/release process, only a small sorbent mass is required; based on system-level estimates, ~1 kg of sorbent is sufficient to meet HVAC demand over a typical driving cycle even under extreme conditions (−10 °C for heating and 50 °C for cooling). Even if integrating an auxiliary energy unit introduces some mass penalty, the associated reduction in HVAC/BTM electricity draw from the traction battery is expected to produce a net-positive impact on driving range. Overall, this demonstrates the feasibility of adopting the e-thermal bank as an auxiliary thermal energy module without imposing a prohibitive performance penalty.

Conclusions

This work introduces the e-thermal bank, an auxiliary energy system designed to extend the driving range of EVs by offloading the HVAC and BTM demands from the main battery pack. This first-of-its-kind, MW-driven TCS system offers high energy and power densities, is fast-charging, and can be recharged concurrently with the main battery—minimizing additional load during driving. To meet stringent performance requirements, we engineered an advanced sorbent material through integrated micro- and macrostructural design. The resulting material demonstrates a record-high sorption capacity of 3.96 g g^{-1} and a material-level energy density of 10 426 kJ kg^{-1} at 90% RH—among the highest reported

values—while maintaining leak-proof and stable operation. This high-performance material has been successfully scaled into a working prototype delivering an energy density of 2135 Wh kg^{-1} and power densities of 2.96 kW kg^{-1} for heating and 3.016 kW kg^{-1} for cooling. The system's high energy density estimates that just 1 kg of sorbent material is sufficient to meet the HVAC needs for a typical driving cycle, even in extreme climates—from −10 °C for heating to 50 °C for cooling.[2] Furthermore, theoretical calculations based on real-world driving conditions predict that integrating the e-thermal bank can extend EV driving range by up to 30% in winter and 20% in summer across most geographic regions. This study offers a scalable and energy-efficient pathway to enhance EV range and performance, particularly under thermally demanding environments, paving the way for broader adoption of electric mobility. Future research will focus on system integration, safety issues, scalability and the practical implementation of the proposed system under real-world operating conditions.

Author contributions

W. A. and Y. L. conceived the idea and designed the research. W. A. performed the experiments and wrote the original manuscript. W. A., M. K., Q. H., and D. L. analyzed the experimental results. J. J. and M. M. contributed to data analysis and visualization. All authors contributed to the discussion. Y. L. supervised the research and edited the manuscript.

Conflicts of interest

W. A., Q. H., and Y. L. are named inventors on a patent application related to this work (UK Patent Application No. 2517030.9). The authors declare no other competing interests.

Data availability

All data relevant to our paper are either provided in the supplementary information (SI) or are available from the authors on request. Supplementary information is available. See DOI: https://doi.org/10.1039/d5mh02273h.

Acknowledgements

This work was financially supported by the Engineering and Physical Sciences Research Council (EPSRC), United Kingdom, through grants EP/V042033/1 and EP/V041665/1. The authors would like to express their sincere thanks to Dr Jie Chen, Dr Tiejun Lu, and Dr Abdalqader Ahmad for their technical support and guidance.

References

1 N. C. Parker, M. Kuby, J. Liu and E. B. Stechel, *Appl. Energy*, 2025, **380**, 125051.
2 S. De Antonellis, L. D. Marocco, G. Tomaino, F. Romano, L. Calabrese and A. Freni, *Next Energy*, 2024, **5**, 100170.
3 J. Guo and F. Jiang, *Energy Convers. Manage.*, 2021, **237**, 114145.
4 M. Steinstraeter, T. Heinrich and M. Lienkamp, *World Electr. Veh. J.*, 2021, **12**, 115.
5 N. Zhang, Y. Lu, S. Kadam and Z. Yu, *Appl. Energy*, 2023, **348**, 121600.
6 C. Cuevas, S. Declaye and V. Lemort, *Adv. Mech. Eng.*, 2019, **11**, 1–13.
7 S. Lei, S. Xin and S. Liu, *J. Power Sources*, 2022, **550**, 232133.
8 M. Wilks, C. Wang, J. Ling-Chin, X. Wang and H. Bao, *Energy Convers. Manage.*, 2023, **291**, 117325.
9 W. Zhao, X. Lin, T. Zhang and Y. Ding, *Carbon Neutrality*, 2024, **3**, 30.
10 S. Saher, S. Johnston, R. Esther-Kelvin, J. M. Pringle, D. R. MacFarlane and K. Matuszek, *Nature*, 2024, **636**, 622–626.
11 Y. Zhang and R. Wang, *Energy Storage Mater.*, 2020, **27**, 352–369.
12 Z. Liu, J. Xu, M. Xu, C. Huang, R. Wang, T. Li and X. Huai, *Nat. Commun.*, 2022, **13**, 193.
13 T. Hatakeyama, N. L. Okamoto, S. Otake, H. Sato, H. Li and T. Ichitsubo, *Nat. Commun.*, 2022, **13**, 1452.
14 S. Chakravarty, W. Hinz, D. Antao and P. J. Shamberger, *Matter*, 2024, **7**, 3608–3624.
15 S.-F. Wu, G.-L. An, W.-G. Pan, T. Yan and L.-W. Wang, *Matter*, 2025, **8**, 101903.
16 A. J. Rieth, A. M. Wright, S. Rao, H. Kim, A. D. LaPotin, E. N. Wang and M. Dinca, *J. Am. Chem. Soc.*, 2018, **140**, 17591–17596.
17 A. Martin, D. Lilley, R. Prasher and S. Kaur, *Energy Environ. Mater.*, 2024, **7**, e12544.
18 P. A. J. Donkers, L. C. Sögütoglu, H. P. Huinink, H. R. Fischer and O. C. G. Adan, *Appl. Energy*, 2017, **199**, 45–68.
19 S. Kiyabu, P. Girard and D. J. Siegel, *J. Am. Chem. Soc.*, 2022, **144**, 21617–21627.
20 M. C. Eberbach, A. I. Shkatulov, H. P. Huinink, H. R. Fischer and O. C. G. Adan, *Microporous Mesoporous Mater.*, 2025, **391**, 113605.
21 S. Wang, A. Stahlbuhk and M. Steiger, *Fluid Phase Equilib.*, 2024, **585**, 114171.
22 J. Aarts, B. van Ravensteijn, H. Fischer, O. Adan and H. Huinink, *Appl. Energy*, 2023, **341**, 121068.
23 J. Aarts, H. Fischer, O. Adan and H. Huinink, *J. Energy Storage*, 2025, **114**, 115726.
24 M. C. Eberbach, H. P. Huinink, A. I. Shkatulov, H. R. Fischer and O. C. G. Adan, *Cryst. Growth Des.*, 2023, **23**, 1343–1354.
25 A. Shkatulov, R. Joosten, H. Fischer and H. Huinink, *ACS Appl. Energy Mater.*, 2020, **3**, 6860–6869.
26 T. Nonnen, H. Preißler, S. Kött, S. Beckert and R. Gläser, *Microporous Mesoporous Mater.*, 2020, **303**, 110239.
27 A. Permyakova, S. Wang, E. Courbon, F. Nouar, N. Heymans, P. D'Ans, N. Barrier, P. Billemont, G. De Weireld, N. Steunou, M. Frère and C. Serre, *J. Mater. Chem. A*, 2017, **5**, 12889–12898.

28 H. Shan, Z. Zeng, X. Yang, P. Poredoš, J. Yu, Z. Chen and R. Wang, *ACS Energy Lett.*, 2023, **8**, 5184–5191.
29 G. Graeber, C. D. Diaz-Marin, L. C. Gaugler, Y. Zhong, B. El Fil, X. Liu and E. N. Wang, *Adv. Mater.*, 2024, **36**, e2211783.
30 J. Aarts, B. van Ravensteijn, H. Fischer, O. Adan and H. Huinink, *Energy*, 2023, **285**, 129540.
31 B. Elahi, D. Salehzadeh, W. M. D. Vos, N. Shahidzadeh, G. Brem and M. Mehrali, *Chem. Eng. J.*, 2024, **500**, 157042.
32 B. G. P. van Ravensteijn, P. A. J. Donkers, R. C. Ruliaman, J. Eversdijk, H. R. Fischer, H. P. Huinink and O. C. G. Adan, *ACS Appl. Polym. Mater.*, 2021, **3**, 1712–1726.
33 T. Yan, T. Li, J. Xu, J. Chao, R. Wang, Y. I. Aristov, L. G. Gordeeva, P. Dutta and S. S. Murthy, *ACS Energy Lett.*, 2021, **6**, 1795–1802.
34 J. Reynolds, N. Koungampillil, J. Elvins, E. Jewell, J. Searle, N. C. Mumford, C. Pleydell-Pearce and R. E. Johnston, *Appl. Therm. Eng.*, 2025, **269**, 126138.
35 J. Aarts, S. de Jong, M. Cotti, P. Donkers, H. Fischer, O. Adan and H. Huinink, *J. Energy Storage*, 2022, **47**, 103554.
36 Y. Jiang, Z. Xu, T. Huang, Y. Liu, F. Guo, J. Xi, W. Gao and C. Gao, *Adv. Funct. Mater.*, 2018, **28**, 1707024.
37 Y. Shao, K. Nie, M. Iliut, F. Box, D. Luan, Y. Shen, W. Wang, W. W. Sampson, I. Dierking and A. Vijayaraghavan, *J. Mol. Liq.*, 2023, **375**, 121341.
38 Z. Zeng, X. Yang, B. Zhao, Z. Chen, K. J. E. Chua and R. Wang, *Energy Environ. Sci.*, 2024, **17**, 800–812.
39 J. Xu, T. Li, T. Yan, S. Wu, M. Wu, J. Chao, X. Huo, P. Wang and R. Wang, *Energy Environ. Sci.*, 2021, **14**, 5979–5994.
40 L. Garzón-Tovar, J. Pérez-Carvajal, I. Imaz and D. Maspoch, *Adv. Funct. Mater.*, 2017, **27**, 1606424.
41 Y. Hou, Z. Sheng, C. Fu, J. Kong and X. Zhang, *Nat. Commun.*, 2022, **13**, 1227.
42 T. X. Li, S. Wu, T. Yan, J. X. Xu and R. Z. Wang, *Appl. Energy*, 2016, **161**, 1–10.
43 C. Zhang, S. Wu, G. An and L. Wang, *Chem. Eng. J.*, 2022, **441**, 136111.
44 M. Zamengo, H. Einaga, Y. Wada and J. Morikawa, *J. Energy Storage*, 2025, **108**, 115195.
45 Y. Zeng, B. Zhang, Y. Fu, F. Shen, Q. Zheng, D. Chalise, R. Miao, S. Kaur, S. D. Lubner, M. C. Tucker, V. Battaglia, C. Dames and R. S. Prasher, *Nat. Commun.*, 2023, **14**, 3229.
46 A. Ahmad and Y. Ding, *Energy Convers. Manage.*, 2021, **247**, 114748.
47 R. Li, W. Wang, Y. Shi, C. T. Wang and P. Wang, *Adv. Mater.*, 2024, **36**, e2209460.
48 W. Lin, X. Yao, N. M. Kumar, W. K. Lo, S. S. Chopra, N. Y. Hau and S. Wang, *Adv. Energy Mater.*, 2024, **14**, 2303470.
49 K. Liu, J. Wang, T. Yamamoto and T. Morikawa, *Appl. Energy*, 2018, **227**, 324–331.
50 M. Senol, I. S. Bayram, Y. Naderi and S. Galloway, *IEEE Access*, 2023, **11**, 39879–39912.